Micro-cracking and incipient shear microstructures at low-strain deformation of Opalinus Clay: Insights from triaxial testing and broad-ion-beam scanning-electron-microscopy (BIB-SEM)

Lisa Winhausen[1], Jop Klaver[2], Joyce Schmatz[2], Guillaume Desbois[3], Janos L. Urai[4], Florian Amann[1],
5 Christoph Nussbaum[5]

[1] Department of Engineering Geology and Hydrogeology, RWTH Aachen University, 52064, Germany
[2] MaP - Microstructures and Pores GmbH, Lochnerstraße 4-20, 52064 Aachen, Germany
[3] Institute of Structural Geology, Tectonics and Geomechanics, RWTH Aachen University, 52064 Aachen, Germany
[4] Institute of Tectonics and Geodynamics, RWTH Aachen University, 52064 Aachen, Germany
10 [5] Federal Office of Topography swisstopo, Route de la Gare 63, 2882 St.-Ursanne, Switzerland

Correspondence to: L. Winhausen (winhausen@lih.rwth-aachen.de)

Abstract. A microphysics-based understanding of mechanical and hydraulic processes in clay shales is required for developing advanced constitutive models, which can be extrapolated to long-term deformation. Although many geomechanical laboratory tests have been performed to characterize the bulk mechanical, hydro-mechanical and failure behaviour of Opalinus Clay,
15 important questions remain about microphysics: How do microstructural evolution and deformation mechanisms control the complex rheology over time scales not accessible in the laboratory. In this contribution, Scanning Electron Microscopy (SEM) was used to image microstructures in an Opalinus Clay sample deformed in an unconsolidated-undrained triaxial compression test at 4 MPa confining stress followed by Argon Broad Ion Beam (BIB) polishing. Axial load was applied (sub-) perpendicular to bedding until the specimen failed. The test was terminated at an axial strain of 1.35%. Volumetric strain measurements
20 showed bulk compaction throughout the compression test. Observations on the cm- to µm-scale showed that deformation localized by forming a network of µm-thick fractures. In BIB-SEM at the grain scale, incipient deformation zones show dilatant inter- and intragranular micro-cracking, granular flow, plastic deformation and bending of phyllosilicate grains, and pore collapse in fossils. Outside these zones, no deformation microstructures were observed indicating localized damage. Thus, microphysics of deformation appear to be controlled by both brittle and ductile processes along preferred orientations.
25 Anastomosing networks of deformation bands develop into the main deformation bands along which the sample fails. Microstructural observations and the stress-strain behaviour were integrated into a deformation model with three different stages of damage accumulation representative for the deformation of the compressed Opalinus Clay sample. Results on the microscale explain how the sample locally dilates while bulk measurement shows compaction, with an inferred major effect on permeability evolution. Comparison with the microstructure of highly strained Opalinus Clay in fault zones shows minor
30 similarity and suggest that during long-term deformation additional solution-precipitation processes operate.

1   Introduction

Due to its low permeability and self-sealing capability, Opalinus Clay (OPA) has been chosen as host rock for nuclear waste disposal in deep geological formations in Switzerland. Major effort has been made to study its mechanical and hydro-
35   mechanical behaviour in laboratory experiments (e.g. Nüesch, 1991; Aristorenas, 1992; Bock, 2010; Amann et al., 2011; Wild et al., 2015, 2018; Favero et al., 2018; Giger et al. 2018). From a geomechanical point of view, the behaviour of OPA is at the transition from a stiff soil to a weak rock. The strain response upon loading suggests a yielding stress threshold that coincides with the onset of dilation. Micro-acoustic measurements on both, the laboratory and field scale suggest that the onset of dilatancy is associated with micro-acoustic events, which is typically observed for brittle rocks (Amann et al. 2011; Wild et al.
40   2015; Amann et al. 2018).

As a consequence of sedimentation, physical compaction, and development of diagenetic bonding (Marschall et al., 2005), OPA shows a well-pronounced bedding and foliation resulting in transversely isotropic hydraulic and mechanical characteristics. Cm-scale lithological heterogeneity and the pronounced microfabric, i.e. preferred grain orientation, govern the macroscopic lamination. Houben et al. 2013 and Houben et al. 2014 give an overview of the microstructure of the pristine
45   material (unfaulted shaly OPA). SEM-based studies (scanning electron microscopy) have shown that the microfabric consists of larger sub-millimetre components embedded in a matrix of subparallel platy clay aggregates (Klinkenberg, 2009; Houben et al., 2013, 2014; Seiphoori et al., 2017).

Typically, the microstructure consists of the following components: Siderite, biogenic calcium carbonate (fossil shells), mica, calcite, organic matter, quartz, pyrite, feldspar and clay matrix. These components can be porous such as the clay matrix,
50   fossils, framboidal pyrite and organic matter or non-porous such as such as quartz-, mica- and calcite grains. The visible void space consists principally of bedding-parallel cracks, pores in the fossils or pyrite and three different pore types in the clay matrix (Houben et al., 2013; Desbois et al., 2009). Based on statistical analysis, the visible pore size can be described by a power-law distribution, which, when extrapolated to pore sizes comparable to the measurement limit of the bulk porosity measurements, it matches with the measured porosity of the shaly facies of OPA of 15.3 % (Houben et al., 2013, 2014) which
55   is slightly lower than petrophysical porosity measured by Busch et al. (2017). Elongated pores in the clay matrix, as well as elongated grains such as micas and calcite clasts are oriented parallel to bedding (Wenk et al., 2008; Houben et al., 2014). The combination of BIB-SEM (broad-ion beam scanning electron microscopy), FIB-n (focused ion beam nano tomography) and STEM (scanning transmission electron microscopy) allows a multi-scale description of the pore structure indicating a more connected pore network parallel to bedding as compared to normal to bedding (Keller et al., 2011, 2013).
60   Microphysics of deformation in clay-rich rocks are complex (e.g. Desbois et al., 2016; Desbois et al., 2017; Schuck et al., 2020). Early macroscopic studies on experimentally deformed shales by compressive loading show that failure is accompanied by shear faulting both across and in-plane of anisotropy, plastic flow or slip along the plane of anisotropy, or kinking (McLamore and Gray, 1967). These processes depend on the confining stress and the orientation of the anisotropy plane in respect to the applied stress. For example, deformation tests on shales from the Wilcox shale formation show that deformation

65   at confining stresses less than 100 MPa is prone to develop macroscopic sharp shear fractures, while experiments at higher confining pressures above 100 MPa reveal macroscopic shear zones with en-enchelon fractures and kink bands following compositional layering (Ibanez and Kronenberg, 1993). Their microscale analyses indicate brittle, dilatant micro-cracking over a wide range of scales where deformation is accompanied by kinking of clay minerals. Hence, the deformation behaviour of shales or clay-rich materials can be brittle, ductile or a combination of both. Underlying micro-mechanisms are cataclasis,

70   granular flow, frictional sliding and crystal plasticity (Morgenstern and Tchalenko, 1967; Handin et al., 1963; Maltman, 1987; Logan et al., 1979; 1987; Wang et al., 1980; Lupini et al., 1981; Rutter et al., 1986; Blenkinsop, 2000; Desbois et al., 2016, Desbois et al., 2017; Schuck et al., 2020).

Holland et al. (2006) presented a model for deformation of shales with a high Brittleness Index (Ingram and Urai, 1999) where initial deformation leads to the formation of dilatant micro-fracture arrays with strong increase in permeability, with

75   progressive deformation and cataclasis of fragments forming a ductile clay gouge and resealing of the fractures.

Microphysical models of phyllosilicate-rich fault gauge for different crustal regimes have been developed using ring shear experiments with rock analogues consisting of mixtures of granular halite and fine-grained muscovite or kaolinite (Bos and Spiers, 2000, 2002). The rheology is controlled by frictional or frictional-viscous behaviour depending on strain rates and the effect of pressure solution. Later, the model was extended by plastic flow of phyllosilicates and the competing processes of

80   shear-induced dilatation and compaction due to pressure solution (Niemeijer and Spiers, 2007).

For OPA, links from structural analyses to deformation mechanisms have been derived using natural outcrops and laboratory experiments. Faulted OPA in outcrops of the Jura mountains indicate discrete shear surfaces with thicknesses of $1 - 4$ µm (Jordan and Nüesch, 1991). These shiny and mirror-like surfaces, i.e. slickenslides, consist of denser packed clay material. They are characterized by a grain size reduction and a preferred alignment of clay aggregates parallel to the shear zone forming

85   R- and Y-shears (cf. Passchier and Trouw, 2005). The dominantly brittle and friction-controlled deformation mechanism is supported by a series of compression tests covering a broad range of ultimate strains (ε up to >20 %) and confining stresses (Nüesch, 1989; Jordan and Nüesch, 1991). The authors interpreted that the experimentally produced R-surfaces act as sliding surfaces on water interlayers and comprise the essential deformation mechanisms. Kaufhold et al. (2016) performed micro-structural analyses using different X-ray computed tomography (CT) techniques with varying resolutions and found two

90   prominent fracture sets in an experimentally deformed OPA under unconsolidated-undrained conditions at 6 MPa confining stress. Detailed investigations in combination with SEM show an oblique-oriented macro-fracture accompanied by small fractures, cracks and the rearrangement of particles. The authors interpret the microstructural deformation as mylonitic shear zone.

Although CT and SEM analysis provide important insights for an advanced understanding of failure processes in OPA, they

95   remain inconclusive at the grain-scale. Currently, only few studies exist which investigate grain-scale processes using high-resolution images. Laurich et al., 2014, 2017 and 2018, analysed the deformation structure from meso- down to grain-scale on samples from the tectonic main fault cross-cutting the underground research lab Mont Terri (URL MT). Results show a network of localised, micron-thick shear zones strongly reduced in porosity, slickensides and scaly clay forming mostly undeformed

microlithons. The formation of gauge is associated to both brittle deformation including micro-fracturing and cataclasis,
100   pressure solution and ductile flow of the clay matrix forming relays which ultimately lead to the formation of scaly clay. The formation of scaly clay has also been modelled experimentally by direct shear test on samples sheared both parallel and normal to bedding direction at various normal stresses (Orellana et al., 2018). Deformation is localised in R-shear planes creating slickenside surfaces and for samples sheared normal to bedding a rotation of the original fabric creating millimetre-sized off-sets along the R-shears.

105   However, there is at this point almost no data published on grain-scale deformation mechanisms and microstructure evolution of OPA in laboratory experiments. Furthermore, existing studies (cf. references above) present deformation structures resulting from shear displacements in the order of metres (fault rock) to centimetres (experimentally deformed samples) resulting in an advanced stage of deformation up to residual or ultimate rock strength. For understanding the rheology during the entire deformation process, earlier stages of deformation and the influence of anisotropy on the grain scale are fundamental. In
110   particular, the knowledge of micro-mechanical deformation and the localization of strain are relevant for the implementation of damage in constitutive models (e.g. Oka et al., 1995; Pietruszszak, 1999; Kimoto et al., 2004; Haghighat and Pietruszczak, 2015).

In this contribution, the deformation structures of a sample were analysed that has been deformed under triaxial stress conditions to peak stress, where damage has been initiated but not reached its residual strength state. We integrate the bulk
115   mechanical failure behaviour under well-defined experimental conditions with the underlying micro-mechanical deformation processes to constrain a micro-mechanical progressive failure model. This work presents a first look and precedes a systematic study of multiple samples deformed at a range of conditions.

2   Material and methods

2.1   Material description

120   A detailed description of the experimental setup, the petrophysical and mechanical results of the sample used in this study can be found in Amann et al., 2012 (their sample #214-38) and will be summarized only briefly in this contribution. The core material, where the sample was extracted from, originated from shaly facies of Opalinus Clay of the Mont Terri Underground Research Laboratory. The typical mass fractions of the main mineralogical components are: (i) clay minerals (50-66%) composed of 2:1 layer and mixed layer silicates (20-30%), and chlorite (7-8%) and kaolinite (20-25%), (ii) quartz (10-20%),
125   (iii) carbonates (8-20%), (iv) iron-rich minerals (4-6 %) and (v) feldspars (3-5%) (Thury and Bossart, 1999; Klinkenberg et al., 2009). The cores were drilled dry utilizing triple-tube core barrels and compressed followed by hermetical sealing in vacuum-evacuated foil (Amann et al., 2012). The cylindrical sample with a length of 179 mm and a diameter or 89 mm was prepared by dry cutting and polishing of end faces using a lathe with a bedding orientation inclined $85 \pm 5°$ to the sample axis. For the water content measurement and calculation of total porosity as well as saturation degree, remaining core pieces were
130   used (ISRM, 1979; Amann et al., 2011) indicating full saturation for the sample used in this study.

2.2 Triaxial testing

The specimen was installed in a triaxial testing machine equipped with two axial and one circumferential strain transducers. The unconsolidated, undrained triaxial compression test (UU test) was performed at constant 4 MPa confining stress and was circumferential-displacement-controlled to give a constant circumferential displacement rate of 0.08 mm/min. The test was
135 terminated right after peak stress indicated by an axial stress drop (Fig. 1). At the end of the test, a total circumferential strain of about -0.60% and a total axial strain of about 1.35% were achieved. At rupture, the axial stress was 15.3 MPa and the axial strain 1.25%. After the test, the specimen remained hermetically sealed in the FEP Fluorocarbon jacket and was stored at room conditions.

2.3 Sample preparation and BIB-SEM

140 For the microstructural analyses, the deformed specimen was removed from the jacket, dried and stabilized with epoxy resin (Fig. 2). Subsequently, the sample was cut dry along the long axis of the specimen and normal to the fracture plane using a diamond saw. Eight sub-samples along the fracture network were cut dry with a micro diamond saw to a size of approximately 2 x 2 x 1 cm^3 (Fig. 3a). The surface of each sub-sample was mechanical pre-polished with SiC grinding papers from P800 to P4000 grit size and glued on a stainless steel sample holder with silver paste. Subsequently, the surfaces of the sub-samples
145 were polished using the BIB surface polishing procedure (Leica TIC3X) using a low incident Ar-ion beam angle (10.5 ° at 7kV for 45 min followed by 4.5° at 5 KV for 4 hours and for some selected sub-samples followed by 4.5° at 5kV for 18 hours, similarly to e.g. Schuck et al., 2020; Laurich et al., 2018; Oelker, 2019).

The BIB-polished surfaces were imaged with SEM (Zeiss Supra 55) after surface coating with a 7 nm thick tungsten layer (Leica EM ACE600). Sample areas imaged with SEM were mapped using mosaic imaging at magnifications ranging from
150 x120 (pixel size of 2,440 nm) to x 30,000 (pixel size of 9.8 nm) depending on the total area and level of details desired. Single images were stitched automatically using the Aztec software (Oxford instrument, version 2.3) to produce large mosaics.

The typical strategy included imaging the total subsample area with BSE detector at low magnification (x110 – x200, 2,730 – 1,508 nm) to provide reference maps for localization of sub-areas. Regions of interests (ROI) were selected and imaged with BSE and SE2 detectors at magnifications ranging from x5,000 to x15,000 (61.8 – 20.1 nm) to provide meso-scale information
155 about the mineral and pore fabrics. Finally, high-level microstructural details down to grain and pore scale at magnifications up to x30,0000 (10.0 nm) are imaged with BSE and SE2 detectors to analyse mineral and pore structures. Pore segmentation and quantitative analyses were performed by applying threshold segmentation of SE2-image using the image processing software ImageJ.

3   Results

3.1   Macroscale observations

160 The deformed specimen showed a fracture network with two fracture sets (Fig. 3b). The first set (marked in green and further referred to as fracture set 1) was oriented oblique to the horizontal by an average angle of 49.5°, and the second fracture set was oriented sub-horizontal and parallel to the bedding with an average angle of 9.8° (marked in pink and further referred as fracture set 2). At the top left corner, the specimen showed a single fracture, which splits into branches at a distance of 2 cm

165 from the top. Towards the tips of these branches, the fractures deflected sub-horizontally along bedding-parallel fractures. The inclination of the fracture set changed from approximately 40° of the single fracture at the top towards the branches by more than 50° in the centre of the sample with respect to the horizontal. The branching fractures displayed an anastomosing pattern forming lens-shaped fragments. Additional oblique fractures sub-parallel to the branching fracture were observed throughout the sample which are not connected to the central branching fracture but show relay connections between the two fracture sets

170 (Fig. 3).

3.2   Microscale observations

Selected regions for microscale observations were located close to the larger, macro-fractures of set 1 (Fig. 3). However, many of the long, high-aperture fractures crossing larger parts of the sample were (presumably) artefacts produced due to unloading and dust accumulation during sawing and mechanical polishing. Additionally, some locations showed secondary gypsum

175 mineralisation caused by chemical reactions during sample storage. Therefore, these regions were excluded from microscale analysis.

The fractures of set 2 and the microstructure within their close vicinity, i.e. the mineral fabric, grain size and pore structure, corresponded to intact shaly OPA samples analysed by Houben et al., 2013 and 2014. These bedding-parallel fractures were typically formed in response to drying, preparation and/or unloading (Houben, 2013; Soe et al., 2009) and were therefore

180 interpreted to have formed during and after unloading the sample. The oblique-oriented fractures of set 1, however, indicated localized deformation. In general, the deformation was presented in form of tensile micro-cracks or in form of elongated zones indicating shearing. Both cases comprised varying local dilatancy.

Micro-cracks were often oblique to bedding with angles in the range of 30° to 45°. Their width was up to a few µm with variable lengths (Fig. 4). The cracks mainly formed in the clay matrix whereas adjacent, larger components, such as shell

185 fragments and quartz grains, remained intact. In a few cases, the cracks crossed larger, elongated mica grains producing intergranular cracks or grain bending (Fig. 4(c),(d)). Locally, multiple dilatant cracks formed an anastomosing network with lens-shaped islands with widths up to 50 µm (Fig. 5(a),(b)). The foliation within these islands, which is indicated by the shape-preferred orientation (SPO) of elongated grains and pores, bended at the edges towards the crack. Some of these deformation structures showed less dilatancy, mostly ductile deformation and a more pronounced shear component (Fig. 5(c)). Here, the

190 SPO of non-clay minerals and clay aggregates was oblique with respect to the bedding and curved according to the shear sense of the micro-crack. Additionally, thin mica grains were bent according to the shear sense or intersected by a crack.

Apart from the micro-cracks and small strain regions, elongated deformation bands of variable widths up to tens of μm thickness and different deformation intensities could be observed. In these zones, structural deformation included a variety of brittle and ductile deformation markers: Disintegrated framboidal pyrite aggregates, broken and fragmented or flattened fossil
195 shells, broken calcite and silica grains, inter- and transgranular fractures, bend and broken mica grains, delamination of clay aggregates and a change of foliation indicated by a rotated SPO of clay aggregates (Fig. 6). In the latter case, the orientation of SPO has rotated by up to 35° leading to a parallel alignment with the elongated deformation zone and, hence, the shear movement.

The deformation bands indicated zones of increased porosity and were usually located in vicinity of the larger macro-fractures.
200 Sometimes narrower bands formed around large, angular and preserved matrix fragments with sizes up to 20 μm. The structure within these bands showed varying deformation intensities. The characteristic microstructure presented a zone where individual grains were separated from the surrounding clay matrix often indicated by porous rims, and clay aggregates as well as pores showed a random distribution resulting in a loss of SPO (Fig.7). These zones with widths of up to 50 μm hosted a variety of deformation markers and showed an increased porosity by rims around larger quartz grains, by the break-up and
205 disintegration of clay particles forming raddle reef pores (Fig. 7(a),(b)) and by the disaggregation of collapsed fossil fragments and pyrite aggregates (Fig.7(c)). Additionally, they presented intra- and intergranular cracks, kinking of mica grains or a curved foliation expressed by the rotation of SPO of clay aggregates and elongated pores. The transition between the deformed and undeformed zone appeared as a sharp boundary.

3.3   Pore size analysis

210 Qualitative observations of increased porosity within the deformation bands were verified by statistical pore size analysis. Figure 8 shows cumulative pore size distributions derived from binary, segmented SE2-images within and outside of the deformation zone for two different subsamples. Cumulative porosity values in the undeformed zones were 2.84 and 4.07 % for subareas from subsamples SS#2 (Fig.8(a)) and SS#8 (Fig.8(b)) and for the deformed zones two subareas for each subsample yielded porosities of 16.13 and 21.16 %, and 8.79 % and 9.84%, respectively. Furthermore, undeformed zones are characterised
215 by a larger portion of smaller pores, i.e. ≤ 0.006 μm^2, and a minor portion of larger pores, i.e. ≥ 0.02 μm^2, compared to the deformed zones.

4   Discussion

4.1   Deformation mechanisms

The two prominent macro-fracture sets were formed due to different processes. Fracture set 1 is associated to shrinkage due
220 to drying when the material is exposed to air. Bedding-parallel crack formation is commonly known at the micro- and

macroscale (e.g. Soe et al., 2009; Ewy, 2015; Fauchille et al., 2016). Additionally, mechanical forces acting to the sample during sample preparation as well as oven-drying and storage between experiment and BIB-SEM analysis can introduce artificial cracks. The microstructure in vicinity of these fractures did not indicate any alteration compared to the microstructure of undeformed OPA and is therefore not associated to damage due to experimental compressive loading. The fracture set 2,

225   however, showed indications of both brittle and ductile deformation, or a combination of both. The general orientation of the macro-cracks with respect to horizontal showed an average inclination of ca. 50° and was consistent with the orientation of micro-cracks (Fig. 4) and elongated deformation bands (Fig. 5,7) showing inclinations between 40° and 55° observed at the microscale. Immediately after the experiment, the sample revealed macroscopic oblique and bedding-parallel side-steps which were connected via relays (Amann et al., 2012). After drying and sample preparation for the SEM analysis, these side-steps

230   appeared on the microscale as tensile fractures along the bedding but could not be distinguished from bedding-parallel desiccation cracks which were ubiquitous within the sample. Indications of shearing along these sidesteps could not be inferred from our SEM analysis.

In general, the deformation of both the clay-rich matrix and larger quartz, calcite and mica grains is brittle, ductile or a combination. On the one hand, grain scale clay splitting, grain abrasion and intra- and intergranular fracturing promote

235   cataclasis. On the other hand, plastic reorientation of clay aggregates and bending of elongated grains indicate structural reworking to enable grain boundary sliding. The former processes suggest a local loss of cohesion whereas the latter process enables the development of a new foliation parallel to the shear direction. The rock rheology is associated to a mixed failure due to the contrasting stiffness of the multi-component minerology and its spatial distribution. Besides many other factors controlling the bulk failure behaviour, e.g. the amount of effective stress, the orientation of applied stresses, temperature and

240   deformation rate (Popp and Salzer, 2006; Giger et al., 2018; Wild and Amann, 2018), our microstructural observations on OPA promote an intermediate tendency to brittle behaviour compared to other clay-rich rocks, e.g. the Callovo-Oxfordian mudrock (COx) from France and the Boom Clay (BC) from Belgium. The deformation mechanism of COx under triaxial compression is mainly associated to cataclastic mechanisms by grain and matrix fracturing, abrasion and comminution (Desbois et al. 2017). In contrast, deformation mechanisms in BC consist of pore collapse outside of the shear zone and grain

245   boundary sliding as well as particle rotation within the shear zone (Oelker, 2019; Schuck et al., 2020). We note here that these experiments were conducted up to axial strains of ca. 6 and 20 %, respectively. The deformation structures and inferred mechanisms can be related to the amount of calcite, which serves as the cementing agent in these rocks (Klinkenberg et al., 2009; Kaufhold et al., 2013). For OPA, a large amount of calcite is part of the fossil shells rather than diagenetic bonding.

Deformation bands showed an increased internal porosity compared to the surrounding microstructure (Fig. 7). The abundant

250   intra- and intergranular fractures, the delamination of clay aggregates creating saddle reef pore structures, and the strained and collapsed fossil fragments within these dilated zones created space required for the particle movement and led to a locally increased porosity. Porosity values based on SE2-image segmentation of different subareas were 4 to 5 times higher inside these deformation bands compared to the intact rock (Fig. 8). The pore size distribution showed a higher amount of smaller pores in the undeformed zone and a higher amount of larger pores within the deformed zone. We note here that the estimated

255 porosity may be underestimated due to the resolution of our SEM-images. However, Houben et al., 2014 showed that porosity upscaling from a power-law distribution function of pore sizes yields porosity values, which are in the range of values determined by e.g. water loss porosity measurements. Our porosity estimations outside of the deformation bands were similar to porosity measurements on undeformed OPA from the shaly facies of MT-URL (Houben et al., 2014) and verify the approach. On the other hand, the porosity may be overestimated as a large portion of strain will be recovered after unloading

260 of the sample. We assume that unloading elasticity is equal in and outside deformation zones and, hence, the ratio of porosity within and outside the deformation bands remains constant. Nevertheless, even a qualitative analysis demonstrates that the deformation bands formed a local increase of porosity

4.2 Damage accumulation during compressive loading

265 The mechanical bulk deformation of OPA was governed by a combination of two processes: Elastic and irreversible inelastic deformation. Elastic deformation was expressed by homogeneous solid component and pore compression. Plastic deformation was governed by damage accumulation in form of localized strains along distinct surfaces or inside grains, but also by homogeneous matrix bulk compaction (Allirot et al., 1977). Both deformations types occurred simultaneously during the deformation in triaxial compression. Besides the fact that elastic strains were mostly recovered after unloading, bulk

270 compression in clay-rich rocks is associated to clay matrix compaction and pore collapse (Schuck et al., 2020). However, matrix compaction remained difficult to image as a large portion of pores in the clay matrix has a size at the nanometre scale (Houben et al., 2014; Hemes et al., 2016; Klaver et al., 2015), which cannot be resolved using a SEM. For the case of localized plastic deformation, the microstructural analysis showed a local damage accumulation in form of i) µm-thin micro-cracks with a strong preferred orientation of approximately 40° towards the maximum principle stress σ_1 (Fig. 3) and ii) wider deformation

275 bands with increased porosity. The formation of loading-parallel, dilatant micro-cracks as response to axial compression is a well-known for brittle-deforming, hard rocks (e.g. Bieniawski, 1967; Scholz, 1968; Tapponier and Brace, 1976). Similarly, micro-cracking during compressive deformation has also been demonstrated for OPA by micro-acoustic emission (Amann et al., 2012) as well as P- and S- wave velocity measurements (Popp and Salzer, 2007) and showed crack initiation long before stress peak. Corkum and Martin (2007) discussed uniaxial and triaxial test on OPA and presented similar results. They

280 associated the opening of micro-cracks to damage by the breaking of diagenetic bonds in tensile failure, which ultimately leads to a degradation in stiffness and strength.

However, the orientation and distribution of micro-cracks remains unknown. Based on our microstructural analysis, the concept of micro-cracking can be applied in slightly modified form compared to the theory previously formulated for hard, brittle rocks: Tensile cracks form as obliquely – instead of vertically – oriented cracks leading to a non-linear increase of bulk

285 radial extension and a simultaneous reduction in stiffness based on the axial strain response. The process of crack nucleation coincides with the onset of volumetric dilation, i.e. the deviation from linearity of the bulk volumetric strain (Amann et. al, 2011), and it is interpreted as a non-localised process within the sample.

Towards an advanced deformation stage, these cracks localise along distinct planes within the sample and ultimately develop to macroscopic shear planes as observed on both hard rocks (Lockner et al., 1992; Tapponier and Brace, 1976) and other shales

290 (Sarout et al., 2017). Our microstructural analysis showed an increased number of micro-cracks in vicinity of the macroscopic shear fracture, which supports the model of crack localisation. Furthermore, anastomosing crack networks (Fig. 4) support the assumption that single tensile-mode cracks growed during progressive deformation, changeed into hybrid-mode with a shear component and coalesced to develop larger deformation bands or, once fully developed, shear zones. The deformation bands are therefore interpreted to have formed from multiple, coalescing micro-cracks as supported by the fact that some immature

295 bands still contain undeformed fragments of the host rock. Adjacent tips of micro-cracks joined by both brittle and ductile deformation mechanisms on the grain scale. Once these deformation bands were established, shear strain localised within them and the internal structure became disrupted. Shear movement along the deformation band boundary could be inferred from bending of clay particles (Fig. 5, 6(c), 8) and the highly strained and stretched fossil shell fragments (Fig. 8(c') and 8(c'')). Furthermore, the internal microstructure within these bands, i.e. the porous rims, the cracks around and through larger particles,

300 and the random distribution of such, indicated cataclastic flow by grain rotation and material destruction. Correlation indicators for absolute shear displacement within and along these zones were missing. However, if strain would have localise within and along these bands, estimations derived from the amount of maximum principal strains during the test and the orientation of the deformation bands would yield in an accommodation of maximum 0.4 % shear strain along these zones.

At the confining stress tested, OPA typically shows a brittle bulk mechanical behaviour with ongoing deformation beyond

305 peak stress resulting in a stress decrease to residual strength (Wild and Amann, 2018; Giger et al., 2018; Favero et al., 2018). The deformation structures presented in this study support the strain softening behaviour and a reducing frictional resistance: Cohesional bonds were partly lost within the observed deformation bands by intergranular fractures and grain rotation, and clay particle rotation led to an alignment parallel to the deformation band enhancing clay-layer sliding. In this regime, we hypothesize that the deformation bands would continuously be sheared and form a macroscopic shear band through the sample

310 in the post peak region (Morgenstern and Tchalenko, 1967).

For cataclastic flow and particle movement within these deformation bands, more space was required which led to a local porosity increase at the confining stress tested. On the other hand, the bulk mechanical behaviour showed a net increase of volumetric strain, i.e. bulk compaction, up and shortly beyond peak stress (Fig.1). This indicates that the matrix compaction was prevailing the bulk deformation process to this stage. At the same time, a local increase of porosity may imply an increased

315 permeability. This is striking and important to note since faulted OPA usually presents a decreased porosity (Laurich et al., 2017) and a reduction in permeability (Bakker and Bresser, 2020). Here, further research is required to investigate the dependency of permeability and porosity evolution with increasing amount of shear stress.

Some structures found in this study, such as the anastomosing crack network, resemble those found in highly strained OPA (Laurich et al., 2017; Orellana et al., 2018) and predict the early stage of Y-shear development. However, highly sheared OPA

320 is characterised by grain size and porosity reduction, and gouge development (Laurich et al., 2017). Similar observations have been made on other clay-rich rocks (e.g. Haines et al., 2013; Holland et al., 2006; Rutter et al., 1986). Therefore,

microstructures and related processes of an experimentally, up to peak-stress strained sample resemble only restrictedly such observed in naturally deformed OPA. Furthermore, the influence of strain amount and rate, pore pressure evolution during deformation, pressure solution and mineral precipitation as well as self-sealing plays an important role (Laurich et al., 2018;
325   Voltolini and Ajo-Franklin, 2020). Ongoing studies on samples loaded to higher strains and under well-established effective consolidation stresses and undrained conditions will address remaining questions associated to the role of pore pressure and make comparison to naturally-deformed OPA more feasible.

4.3   Micro-mechanical model

For the deformation of OPA under differential compressive load, we propose the following deformation mechanisms based on
330   our microstructural observations in combination with the bulk mechanical behaviour (Fig. 9): In the early stage of differential loading, the sample is subjected to axial shortening and elastic compression up to a differential stress of approximately 2 MPa. From stage (1), yielding starts caused by the formation of cracks and the related reduction of stiffness. These cracks form in the whole sample with preferred orientations crossing the bedding and a higher density in the centre. The non-linear increase of volumetric strain indicates a more abundant crack formation in the beginning at lower axial strains. At stage (2), these cracks
335   coalesce to create networks forming damage zones with widths in the range of 20 to 50 µm. Clay bending indicates a coexistence of brittle and ductile deformation processes due to the contrasting mineral rheology. When peak stress is reached and slightly exceeded at stage (3), shearing initiates and deformation bands begin to develop with distinct boundaries to the undeformed host rock. These damage zones are characterised by both brittle and ductile deformation in form of matrix cataclasis and reorientation of mineral fabric. Locally, these zones are characterised by increased porosity due to strained and
340   crushed fossil shells, rotated calcite and quartz clasts and delamination of clay particles forming saddle reef pores. We hypothesise that with ongoing deformation shear strain will localise along a macroscopic shear band cross-cutting the sample with a reduction in porosity and grain sizes.

5   Implications and conclusions

We derived a deformation model for Opalinus Clay based on a sample that has been deformed in a triaxial test and whose post-
345   experimental microstructure was analysed using BIB-SEM. The bulk mechanical behaviour was related to the micro-physical processes, which are controlled by a combination of brittle and ductile deformation. The micro-mechanical damage in OPA consists of obliquely oriented single and coalescing micro-cracks as well as up to 50 µm-thick deformation bands pointing to deformation processes such as pore collapse, grain rotation and the rearrangement of clay aggregates due to bending and shear straining. Even though the pre-peak bulk volumetric strain showed a compacting behaviour, the microstructure was
350   characterised by dilatant cracks and a local increase in porosity in the deformed zones. Consequently, the accumulation of damage upon compression created additional path ways for fluid flow which can increase the permeability of the rock. At this point, experimentally, up to peak stress deformed OPA showed only few similarities with naturally deformed OPA.

The results of this study support more recent efforts (e.g. Pardoen et al., 2020; Jameei and Pietruszczak, 2021) to implement damage in constitutive models for modelling OPA or similar clay shales, which allow reproducing local porosity and permeability changes due to crack formation, crack coalescence, and the development of shear zones. Further studies on samples tested to larger axial strains on consolidated-undrained samples will test our model of strain localisation and pore space reduction. Furthermore, this will include the role of pore pressure development during deformation, and it will offer the possibility to properly compare experimentally and naturally-deformed OPA.

Data availability. High-resolution BIB-SEM images for this paper can be found in the supplement.

Competing interests. The authors declare that they have no conflict of interest.

Author contributions. GD and JK performed sample preparation and BIB-SEM microscopy. LW wrote the text with contributions from all co-authors. All co-authors contributed to the discussion.

Acknowledgements. We would like to thank Swisstopo for the financial support.

6   References

Allirot, D., Boehler, J. P., and Sawczuk, A.: Irreversible deformations of an anisotropic rock under hydrostatic pressure, Int. J. Rock Mech. Min. Sci. Geomech. Abstr., Vol. 14, No. 2, pp. 77-83, Pergamon, 1977

Amann, F., Button, E. A., Evans, K. F., Gischig, V. S., and Blümel, M.: Experimental study of the brittle behavior of clay shale in rapid unconfined compression. Rock Mech. Rock Eng., 44(4), 415-430, 2011

Amann, F., Kaiser, P., and Button, E. A.: Experimental study of brittle behavior of clay shale in rapid triaxial compression, Rock Mech. Rock Eng, 45(1), 21-33, 2012

Amann, F., Wild, K. M., Loew, S., Yong, S., Thoeny, R., and Frank, E.: Geomechanical behaviour of Opalinus Clay at multiple scales: results from Mont Terri rock laboratory (Switzerland). In Mont Terri Rock Laboratory, 20 Years (pp. 153-173). Birkhäuser, Cham., 2018

Aristorenas, G. V.: Time-dependent behavior of tunnels excavated in shale, Doctoral dissertation, Massachusetts Institute of Technology. 1992

Bakker, E., and de Bresser, J. H.: Anisotropic transport and frictional properties of simulated clay-rich fault gouges, Solid Earth Discussions, 1-25, 2020

Bieniawski, Z. T.: Mechanism of brittle fracture of rock: part I—theory of the fracture process, Int. J. Rock Mech. Min. Sci. Geomech. Abstr., Vol. 4, No. 4, pp. 395-406, Pergamon, 1967

Blenkinsop, T.: Deformation Microstructures and Mechanisms in Minerals and Rocks. Springer, p. 163, 2000

Bock, H., Dehandschutter, B., Martin, C.D., Mazurek, M., De Haller, A., Skoczylas, F. and Davy, C.: Self-sealing of fractures in argillaceous formations in the context of geological disposal of radioactive waste, ISBN 978-92-64-99095-1, 2010.

385   Bos, B., Peach, C. J., and Spiers, C. J.: Frictional-viscous flow of simulated fault gouge caused by the combined effects of phyllosilicates and pressure solution, Tectonophysics, 327(3-4), 173-194, 2000

Bos, B., and Spiers, C. J.: Frictional-viscous flow of phyllosilicate-bearing fault rock: Microphysical model and implications for crustal strength profiles, J. Geophys. Res. Solid Earth, 107(B2), ECV-1, 2002

Busch, A., Schweinar, K., Kampman, N., Coorn, A., Pipich, V., Feoktystov, A., Leu, L., Amann-Hildenbrand, A. and
390   Bertier, P.: Determining the porosity of mudrocks using methodological pluralism. Geological Society, London, Special Publications, 454(1), 15-38, 2017

Corkum, A. G., and Martin, C. D.: The mechanical behaviour of weak mudstone (Opalinus Clay) at low stresses, Int. J. Rock Mech. Min. Sci., 44(2), 196-209, 2007

Desbois, G., Urai, J. L., and Kukla, P. A.: Morphology of the pore space in claystones–evidence from BIB/FIB ion
395   beam sectioning and cryo-SEM observations, eEarth Discussions, 4(1), 1-19, 2009

Desbois, G., Hemes, S., Laurich, B., Houben, M., Klaver, J., Höhne, N., Urai, J.L., Viggiani, G. and Bésuelle, P.: Investigation of microstructures in naturally and experimentally deformed reference clay rocks using innovative methods in scanning electron microscopy, The Clay Minerals Society Workshop Lectures, 21, Chapter 1, 1-14. DOI: 10.1346/CMS-WLS-21.1, 2016

400   Desbois, G., Höhne, N., Urai, J.L., Bésuelle, P. and Viggiani, G.: Deformation in cemented mudrock (Callovo-Oxfordian Clay) by microcracking, granular flow and phyllosilicate plasticity: insights from triaxial deformation, broad ion beam polishing and scanning electron microscopy, Solid Earth, 8, 291-305. Doi: 10.5194/se-8-291-2017, 2017

Ewy, R. T.: Shale/claystone response to air and liquid exposure, and implications for handling, sampling and testing, Int. J. Rock Mech. Min., 80, 388-401, 2015

405   Fauchille, A. L., Hedan, S., Valle, V., Pret, D., Cabrera, J., and Cosenza, P.: Multi-scale study on the deformation and fracture evolution of clay rock sample subjected to desiccation, Appl. Clay Sci., 132, 251-260, 2016

Favero, V., Ferrari, A., and Laloui, L.: Anisotropic behaviour of opalinus clay through consolidated and drained triaxial testing in saturated conditions, Rock Mech. Rock Eng., 51(5), 1305-1319, 2018

Giger, S. B., Ewy, R. T., Favero, V., Stankovic, R., and Keller, L. M.: Consolidated-undrained triaxial testing of
410   Opalinus Clay: Results and method validation. Geomechanics for Energy and the Environment, 14, 16-28, 2018

Haghighat, E., and Pietruszczak, S.: On modeling of discrete propagation of localized damage in cohesive-frictional materials. Int. J. Numer. Anal. Methods Geomech., 39(16), 1774-1790, 2015

Haines, S. H., Kaproth, B., Marone, C., Saffer, D., and Van der Pluijm, B.: Shear zones in clay-rich fault gouge: A laboratory study of fabric development and evolution. J. Struc. Geol., 51, 206-225, 2013

415 Handin, J., Hager Jr, R. V., Friedman, M., and Feather, J. N.: Experimental deformation of sedimentary rocks under confining pressure: pore pressure tests, AAPG Bulletin, 47(5), 717-755, 1963

Hemes, S., Desbois, G., Klaver, J., and Urai, J. L.: Microstructural characterisation of the Ypresian clays (Kallo-1) at nanometre resolution, using broad-ion beam milling and scanning electron microscopy. Neth. J. Geosci., 95(3), 293-313, 2016

Holland, M., Urai, J. L., van der Zee, W., Stanjek, H., and Konstanty, J.: Fault gouge evolution in highly 420 overconsolidated claystones, J. Struc. Geol., 28(2), 323-332, 2006

Houben, M.E., Desbois, G. and Urai, J.L.: Pore morphology and distribution in the shaly facies of Opalinus Clay (Mont Terri, Switzerland): Insights from representative 2D BIB-SEM investigations on mm to nm scale, Appl. Clay Sci., 71: 82-97, 2013

Houben, M., Desbois, G. and Urai, J.L.: A comparative study of representative microstructures in shaly and sandy 425 facies of Opalinus Clay (Mont Terri, Switzerland) inferred from BIB-SEM and MIP methods, Mar. Pet. Geol., 49, 143-161, 2014

Ibanez, W. D., and Kronenberg, A. K.: Experimental deformation of shale: Mechanical properties and microstructural indicators of mechanisms, Int. J. Rock Mech. Min. Sci. Geomech. Abstr., 30, 7, pp. 723-734, Pergamon, 1993

Ingram, G. M., and Urai, J.L.: Top-seal leakage through faults and fractures: the role of mudrock properties. Geological 430 Society, London, Special Publications, 158(1), 125-135, 1999

ISRM: Suggested Methods for Determining Water Content, Porosity, Density, Absorption and Related Properties and Swelling and Slake-Durability Index Properties, Int. J. Rock Mech. Min., 16, 141–156, 1979.

Jameei, A.A., and Pietruszczak, S.: On the hydromechanical interaction during propagation of localized damage on rocks. Minerals, 11 (162), 2021

435 Jordan, P., and Nüesch, R.: Deformational behavior of shale interlayers in evaporite detachment horizons, Jura overthrust, Switzerland. J. Struc. Geol., 11(7), 859-871, 1989

Kaufhold, A., Halisch, M., Zacher, G., and Kaufhold, S.: X-ray computed tomography investigation of structures in Opalinus Clay from large-scale to small-scale after mechanical testing. Solid Earth, 7(4), 1171-1183, 2016

Keller, L. M., Holzer, L., Wepf, R., Gasser, P., Münch, B., and Marschall, P.: On the application of focused ion beam 440 nanotomography in characterizing the 3D pore space geometry of Opalinus clay, Phys. Chem. Earth, Parts A/B/C, 36(17-18), 1539-1544, 2011

Keller, L. M., Schuetz, P., Erni, R., Rossell, M. D., Lucas, F., Gasser, P., and Holzer, L.: Characterization of multi-scale microstructural features in Opalinus Clay, Microporous and mesoporous materials, 170, 83-94, 2013

Kimoto, S., Oka, F., and Higo, Y.: Strain localization analysis of elasto-viscoplastic soil considering structural
445   degradation, Compt. Method. Appl. M., 193(27-29), 2845-2866, 2004

Klaver, J., Hemes, S., Houben, M., Desbois, G., Radi, Z. and Urai, J.L.: The connectivity of pore space in mudstones: insights from high pressure Wood's Metal Injection, BIB-SEM imaging and Mercury Intrusion Porosimetry, Geofluids, 2015

Klinkenberg, M., Kaufhold, S., Dohrmann, R., and Siegesmund, S.: Influence of carbonate microfabrics on the failure strength of claystones, Eng. Geol., 107(1-2), 42-54, 2009

450   Laurich, B., Urai, J. L., Desbois, G., Vollmer, C., and Nussbaum, C.: Microstructural evolution of an incipient fault zone in Opalinus Clay: Insights from an optical and electron microscopic study of ion-beam polished samples from the Main Fault in the Mt-Terri Underground Research Laboratory, J. Struc. Geol., 67, 107-128, 2014

Laurich, B., Urai, J. L., and Nussbaum, C.: Microstructures and deformation mechanisms in Opalinus Clay: Insights from scaly clay from the Main Fault in the Mont Terri Rock Laboratory (CH), Solid Earth, 8(1), 27-44, 2017

455   Laurich, B., Urai, J. L., Vollmer, C., and Nussbaum, C.: Deformation mechanisms and evolution of the microstructure of gouge in the Main Fault in Opalinus Clay in the Mont Terri rock laboratory (CH), Solid Earth, 9(1), 1-24, 2018

Lockner, D.A., Moore, D.E. and Reches, Z.: Microcrack interaction leading to shear fracture, In: Tillerson and Wawersik (eds) 33rd US Rock Mechanics Symposium 908–816, 1992

Logan, J.M. and Rauenzahn, K.A.: Frictional dependence of gouge mixtures of quartz and montmorillonite on velocity,
460   composition and fabric, Tectonophysics, 144, 87–108, 1987

Logan, J.M., Friedman, M., Higgs, N., Dengo, C. and Shimamoto, T.: Experimental studies of simulated gouge and their application to studies of natural fault zones, Open File Report, In: Proceedings of Conference VIII on Analysis of Actual Fault Zones in Bedrock, US Geological Survey, pp. 79–1239, 1979

Lupini, J.F., Skinner, A.E. and Vaughan, P.R.: The drained residual strength of cohesive soils, Geotechnique 31, 181–
465   213.

Maltman, A.: Shear zones in argillaceous sediments - an experimental study, Spec. Pubis geol. Soc. Lond. 29, 77-87, 1987

Marschall, P., Horseman, S., and Gimmi, T.: Characterisation of gas transport properties of the Opalinus Clay, a potential host rock formation for radioactive waste disposal, Oil Gas Sci. Technol., 60(1), 121-139, 2005

470   McLamore, R., and Gray, K. E.: The mechanical behavior of anisotropic sedimentary rocks, J. Eng. Ind. Feb 1967, 89(1): 62-73, 1967

Morgenstern, N. R., and Tchalenko, J. S.: Microscopic structures in kaolin subjected to direct shear, Geotechnique, 17, 309–328, 1967

Niemeijer, A. R., and Spiers, C. J.: A microphysical model for strong velocity weakening in phyllosilicate-bearing fault

475   gouges. Journal of Geophysical Research: Solid Earth, 112(B10), 2007

Nüesch, R.: Das mechanische Verhalten von Opalinuston, Doctoral dissertation, ETH Zurich, 1991

Oelker, A.: Deformation properties of Boom Clay: Implementation of a multi-scale concept, PhD Thesis, RWTH Aachen, 2019, https://publications.rwth-aachen.de/record/771048

Oka, F., Adachi, T., and Yashima, A: A strain localization analysis using a viscoplastic softening model for clay. Int-

480   J. Plast, 11(5), 523-545, 1995

Orellana, L. F., Scuderi, M. M., Collettini, C., and Violay, M.: Frictional properties of Opalinus Clay: Implications for nuclear waste storage, J. Geophys. Res. Solid Earth, 123(1), 157-175, 2018

Pardoen, B., Bésuelle, P., Dal Pont, S., Cosenza, P., and Desrues, J.: Accounting for small-scale heterogeneity and variability of clay rock in homogenised numerical micromechanical response and microcracking, Rock Mech Rock Eng, 53(6),

485   2727-2746, 2020

Passchier, C. W., and Trouw, R. A.: Microtectonics. Springer Science & Business Media, 2005

Pietruszczak, S.: On homogeneous and localized deformation in water-infiltrated soils, Int. J. Damage Mech., 8(3), 233-253, 1999

Popp, T., and Salzer, K.: Anisotropy of seismic and mechanical properties of Opalinus clay during triaxial deformation

490   in a multi-anvil apparatus, Phys. Chem. Earth, Parts A/B/C, 32(8-14), 879-888, 2007

Rutter, E. H., Maddock, R. H., Hall, S. H., and White, S. H.: Comparative microstructures of natural and experimentally produced clay-bearing fault gouges, Pure Appl. Geophys. approx., 124(1), 3-30, 1986

Sarout, J., Le Gonidec, Y., Ougier-Simonin, A., Schubnel, A., Guéguen, Y., and Dewhurst, D. N.: Laboratory micro-seismic signature of shear faulting and fault slip in shale. Phys. Earth Planet. Inter., 264, 47-62, 2017

495   Scholz, C. H.: Experimental study of the fracturing process in brittle rock. J. Geophys. Res. Solid Earth, 73(4), 1447-1454, 1968

Schuck B., Desbois G. and Urai J.L: Grain-scale deformation mechanisms and evolution of porosity in experimentally deformed Boom Clay, J. Struc. Geol., 130, 103894, 2020

500   Seiphoori, A., Whittle, A. J., Krakowiak, K. J., and Einstein, H. H.: Insights into diagenesis and pore structure of opalinus shale through comparative studies of natural and reconstituted materials, Clay Clay Miner., 65(2), 135-153, 2017

Soe, A. K. K., Osada, M., Takahashi, M., and Sasaki, T.: Characterization of drying-induced deformation behaviour of Opalinus Clay and tuff in no-stress regime, Environ. Geol., 58(6), 1215-1225, 2009

Tapponier, P., and Brace, W. F.: Development of stress induced micro-cracks in Westerly granite: Int. J. Rock Mech. Min. Sci., v. 13, 1976

505   Thury, M., and Bossart, P.: The Mont Terri rock laboratory, a new international research project in a Mesozoic shale formation, in Switzerland, Eng. Geol., 52(3-4), 347-359, 1999

Voltolini, M., and Ajo-Franklin, J.: Evolution of propped fractures in shales: the microscale controlling factors as revealed by in situ X-Ray microtomography, J. Pet. Sci. Eng, 188, 106861, 2020

Wang, C., Mao, N. and Wu, F. T.: Mechanical properties of clays at high pressure, J. geophys. Res. 85, 1462-1468, 510   1980

Wenk, H. R., Voltolini, M., Kern, H., Popp, T., and Mazurek, M.: Anisotropy in shale from Mont Terri, The Leading Edge, 27(6), 742-748, 2008

Wild, K. M., Wymann, L. P., Zimmer, S., Thoeny, R., and Amann, F.: Water retention characteristics and state-dependent mechanical and petro-physical properties of a clay shale, Rock Mech. Rock Eng., 48(2), 427-439, 2015

515   Wild, K. M., and Amann, F.: Experimental study of the hydro-mechanical response of Opalinus Clay–Part 1: Pore pressure response and effective geomechanical properties under consideration of confinement and anisotropy, Eng. Geol., 237, 32-41, 2018

7   FIGURES
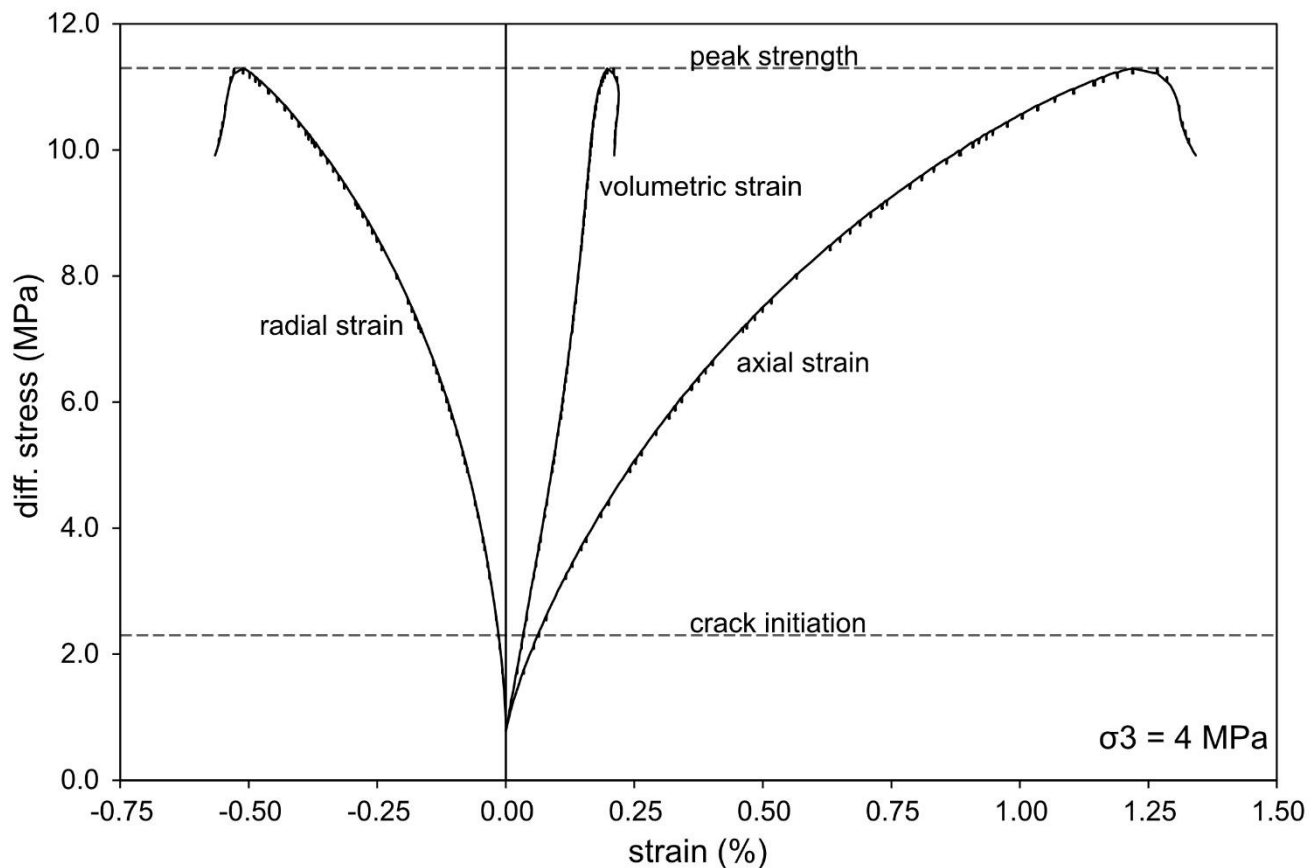
520

Figure 1: Stress versus strain development during the shearing phase. The shearing was conducted circumferential-displacement-controlled and at constant confining stress of 4 MPa. Peak stress was reached at 11.3 MPa differential stress and crack initiation was observed at 2.3 MPa. The volumetric strain curve indicated bulk compaction over the entire experiment.

525
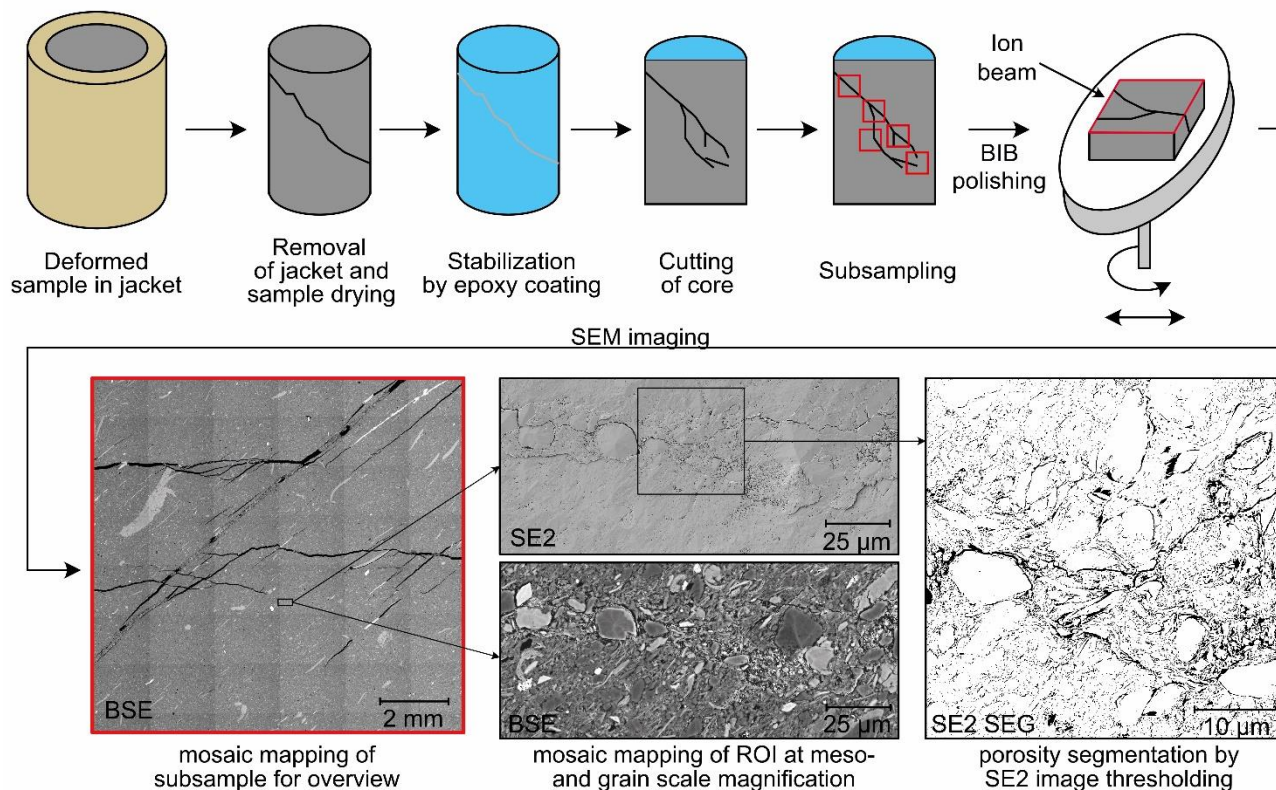
Figure 2: Methodology and sample preparation for the BIB-SEM: After dismantling and sample stabilization by epoxy resin, the sample was cut normal to the fracture plane. Subsampling followed on selected regions of interest (red boxes) which were subjected to ion beam polishing. Finally, BSE-SEM micrographs were taken at low magnifications (110x to 200x) and detailed high resolution SE2- and BSE-SEM images were produced from regions of interest. Pore segmentation was carried out by threshold segmentation of SE2 images.

530
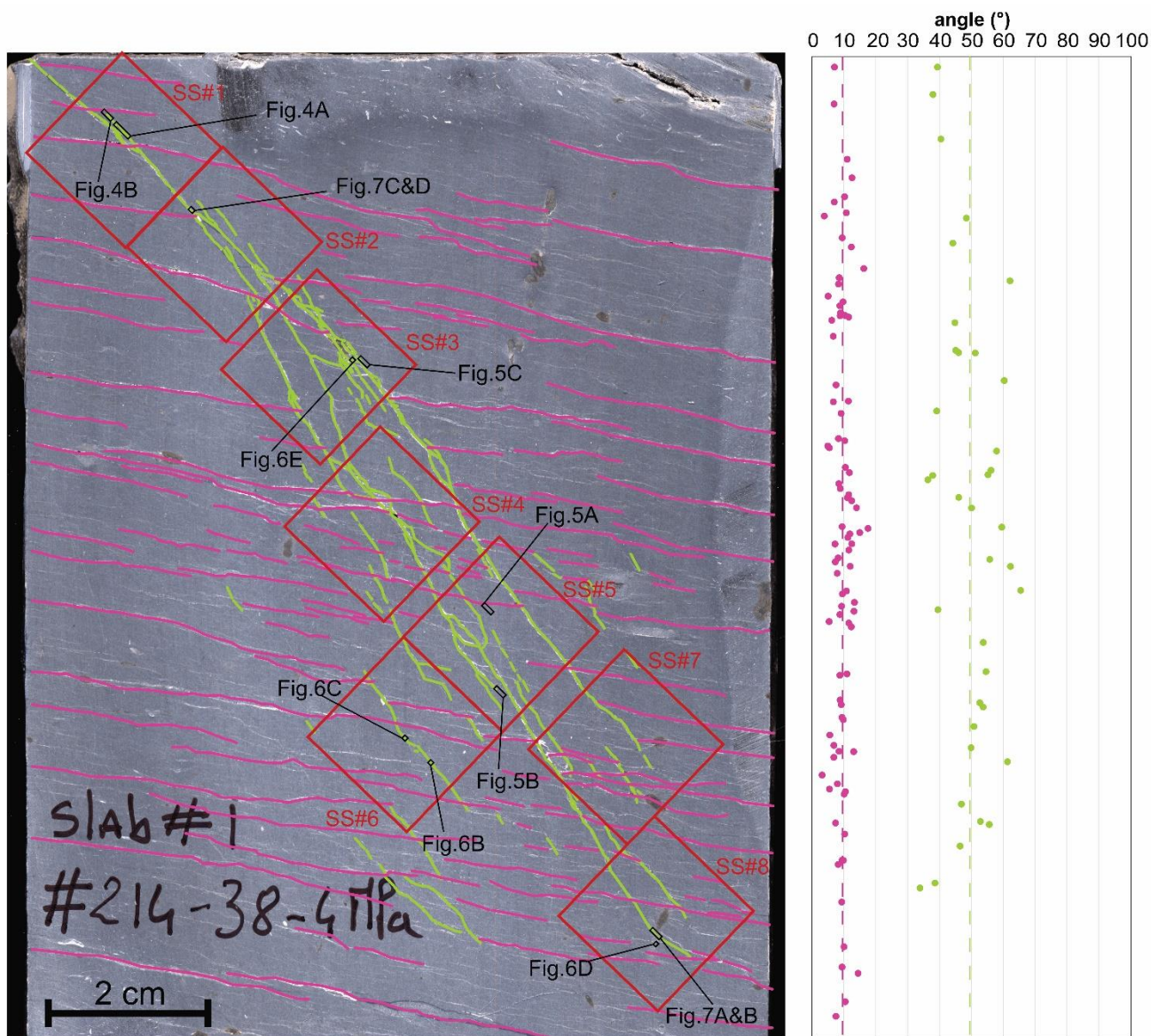
Figure 3: Macroscopic observations of the deformed sample. Red boxes indicate the location of the subsamples and black boxes show the selected regions of interest for large mosaic maps at meso- and grain scale magnifications. Macroscopic mapped fracture network showed two fracture sets: The oblique oriented fracture set (green) showed a branching pattern and had an average inclination angle of 49.5° whereas the sub-horizontal fractures (pink) were inclined by 9.8° in respect to horizontal. Angles of mapped fracture set 2 along the sample length showed a slight increase towards the centre of the sample; the angles of fracture set 1 were consistent throughout the entire sample.

535

540
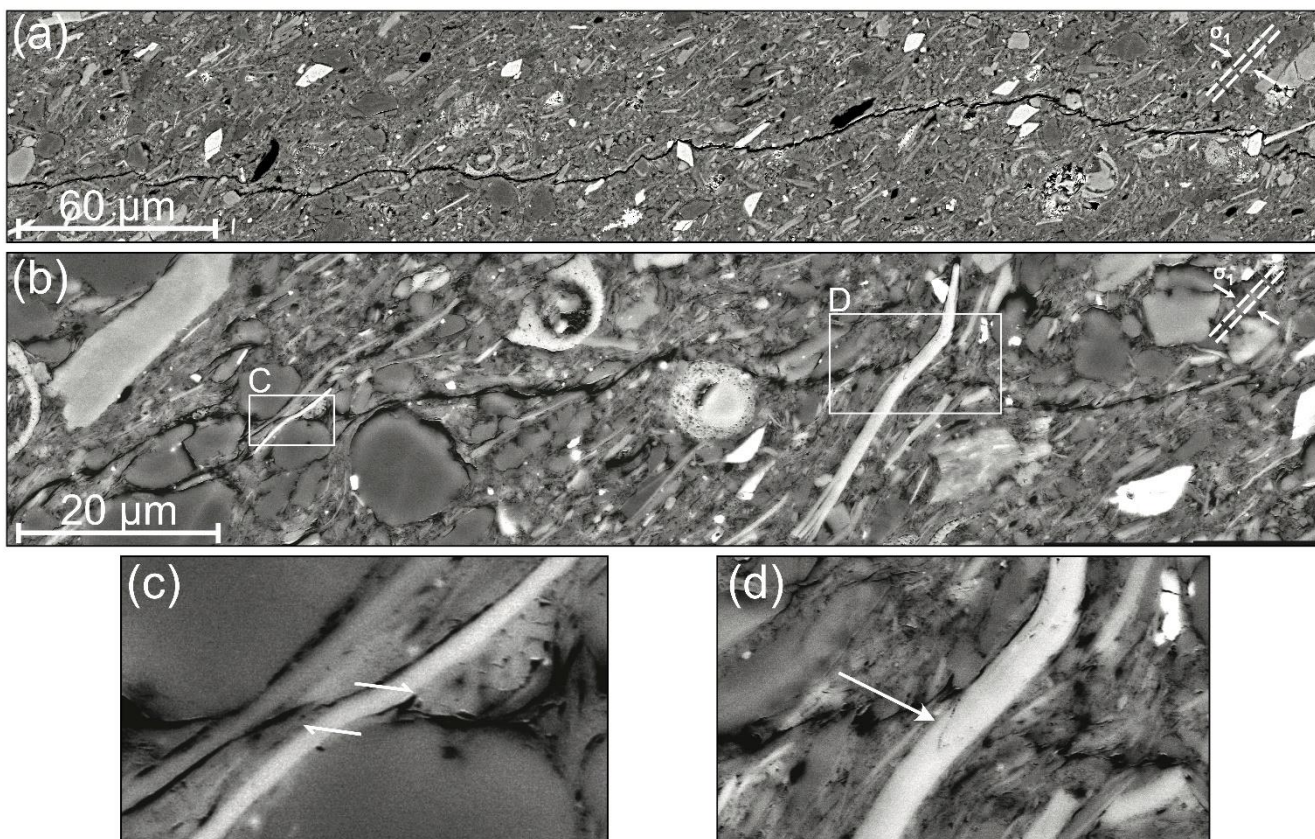
Figure 4: BIB-SEM micrographs (BSE-) showing micro-cracks of variable sizes with apertures of a few µm, which cross the bedding obliquely. Cracks were forming along larger grains (a) or cross elongated mica grains (b) by either creating shear displacements (c) or brittle transgranular fractures (d).

545
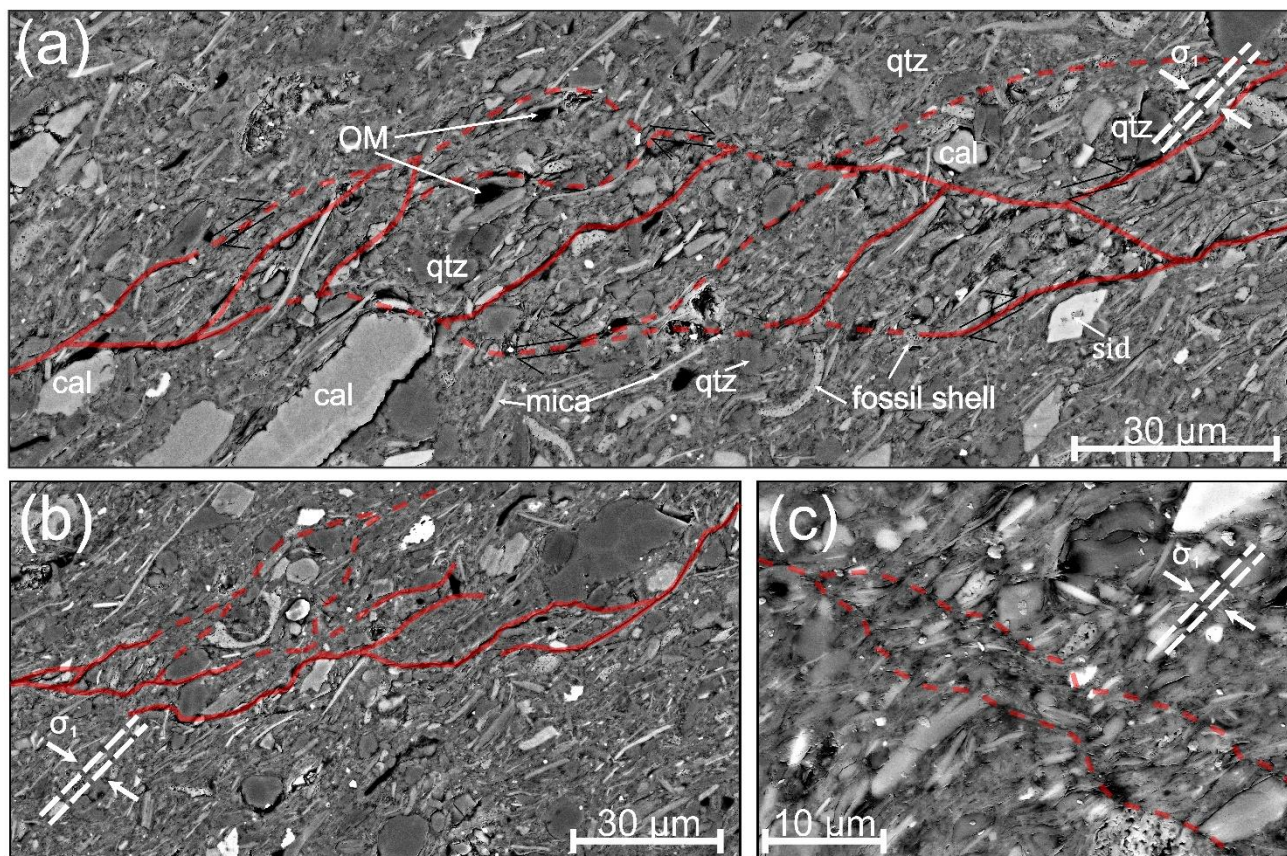
Figure 5: BIB-SEM (BSE-) micrographs showing typical deformation structures associated to both brittle and ductile deformation. Red lines indicate strain localization in form of fractures (a,b) or lineations of shear displacement (c). (a) anastomosing intergranular cracks with apertures of some µm formed lense-shaped islands whereas some grains displayed intragranular fractures. (b) shows cracks with intergranular porosity which formed a not fully-developed network with minor indications of ductile deformation. (c) shows a deformation band with low porosity and predominantly ductile deformation indicated by the change of particle alignments.

550
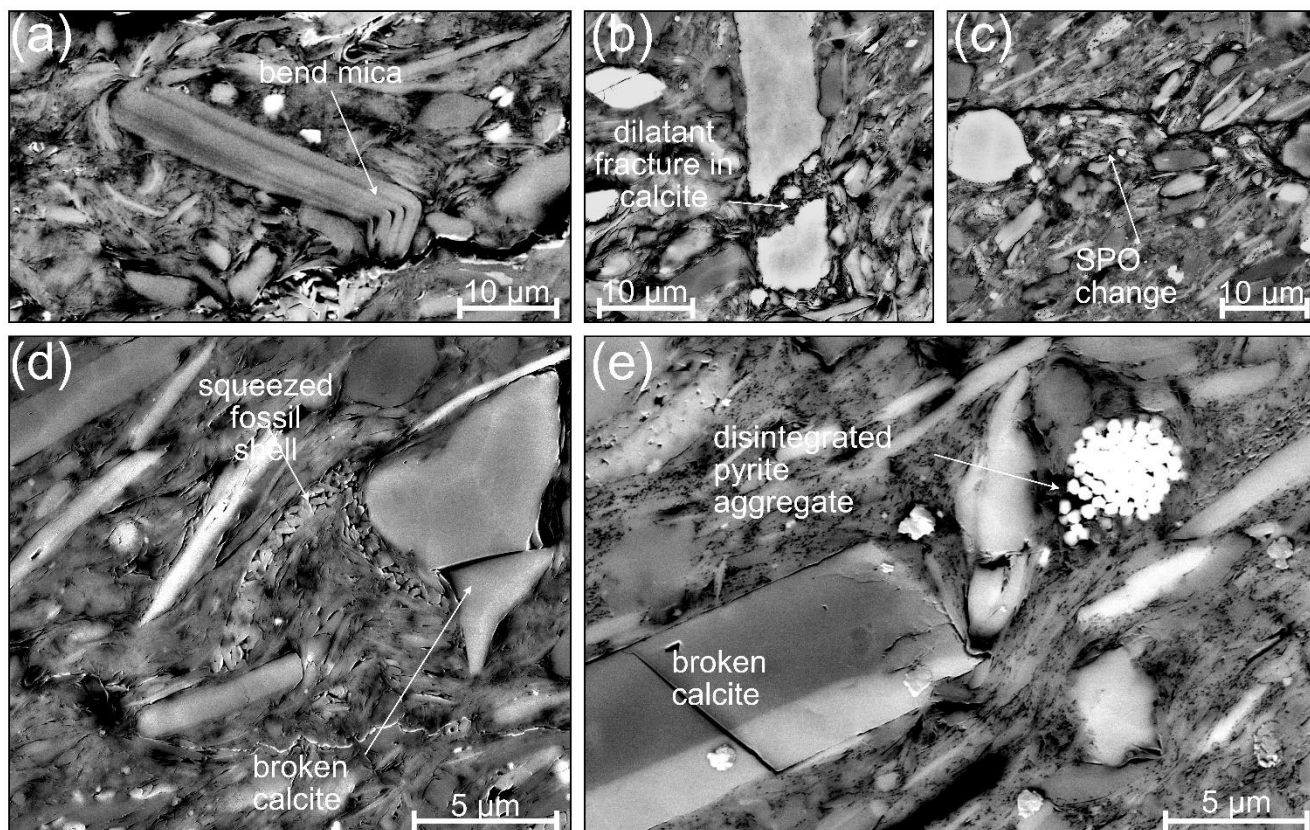
Figure 6: BIB-SEM (BSE-)micrographs presenting different deformation markers: Bend and split mica grain (a), dilatant fracturing of calcite grain and matrix fill (b), change of shape-preferred orientation (SPO) of clay aggregates and elongated minerals (d) squeezed and broken fossil shell, broken calcite gain (d), broken calcite grain and disintegrated pyrite aggregate (e).
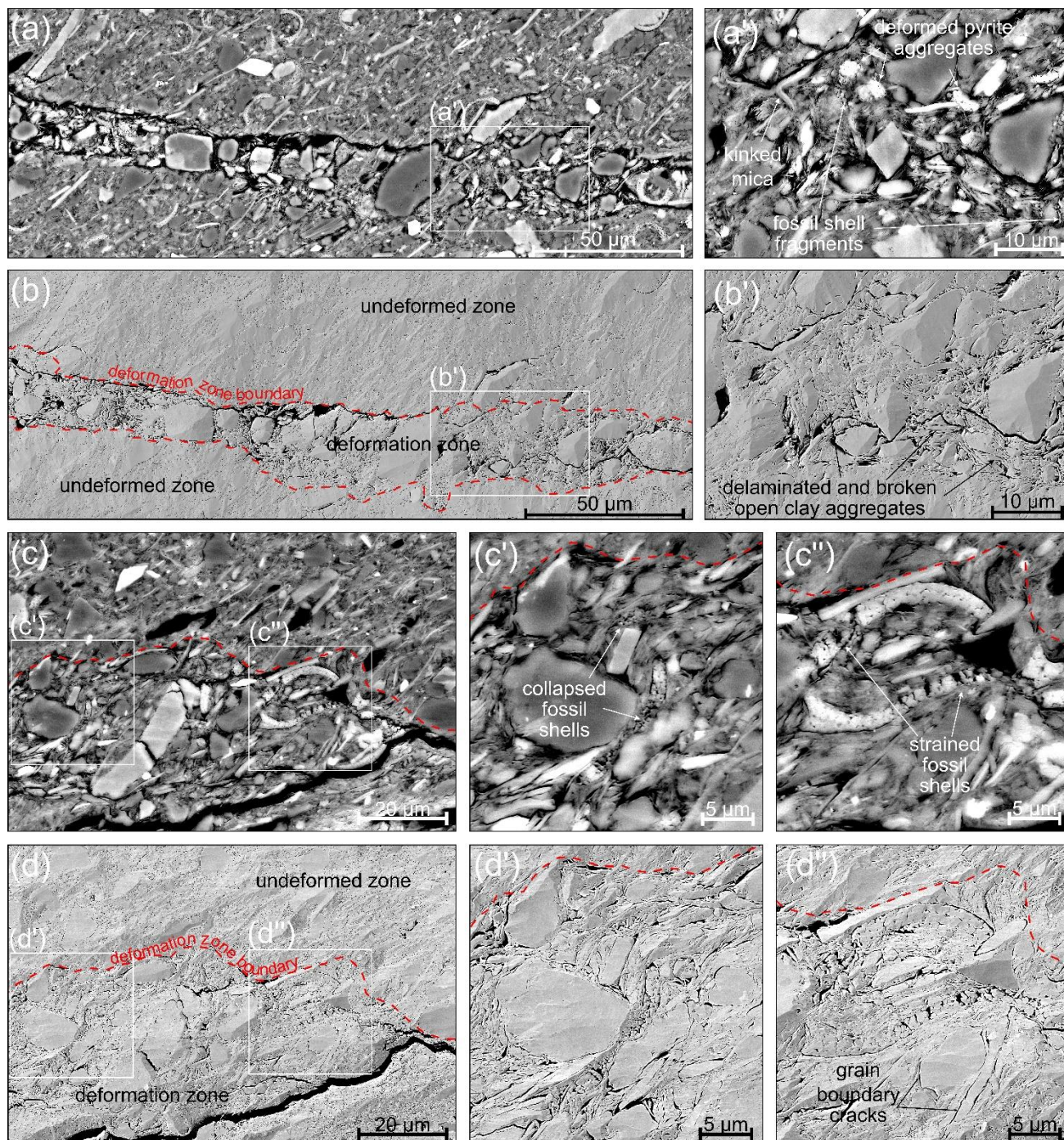
565   **Figure 7: BIB-SEM micrographs showing a zone of increased porosity. (a, a', a'') and (c, c',c'') are BSE-images indicating the grain structures within the dilatant zone of up to 25 µm thickness. The detailed micrograph (a') shows typical strain indicators such as kinked mica, deformed pyrite aggregates and remnants of fossil shells. (b) and (b') are SE2-images showing the pore structure with considerably increased porosity along and within the deformation zone, and the delamination of clay aggregates at higher**

570 magnification. (c) and (c',c'') present intragranular fractures and strained as well as collapsed fossil shells. SE2-image (d) shows an increased number of fractures within the deformation zone, as well as increased pore space in collapsed shell fragments and clay aggregates (d'). (d'') displays grain boundary cracks which appear as porous rims around quartz grains.
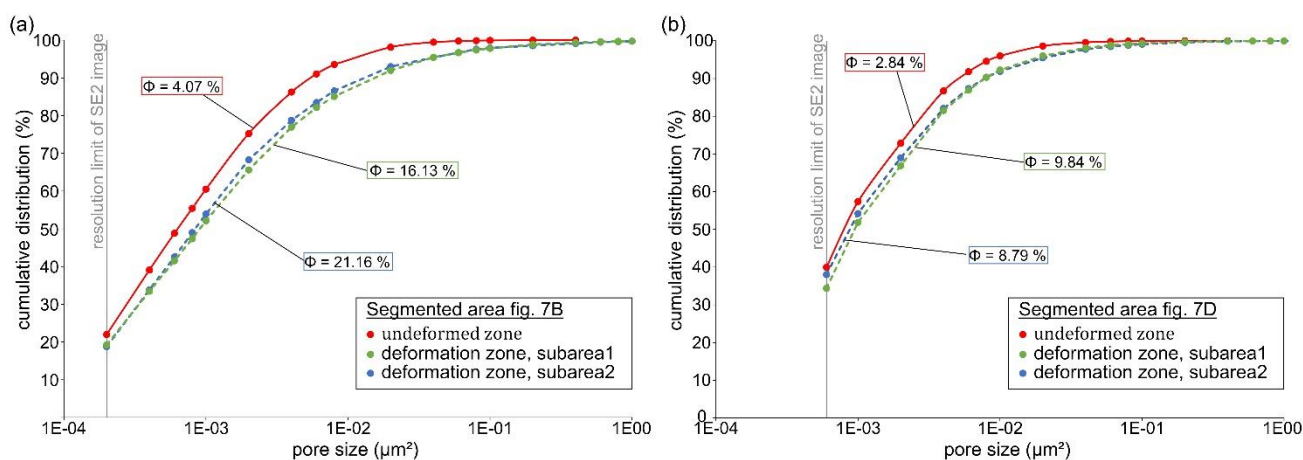
Figure 8: Pore size distributions of undeformed and deformed zones based on SE2-image segmentation from Fig. 7(b) and 7(d).
575 **Deformed zones present an increased porosity by a factor of 4 to 5, and show a higher portion of larger pores. Note that porosities estimated from SEM-image segmentation are underestimated due to the limited image resolution of 2E-04 µm² and 6E-04 µm², respectively.**
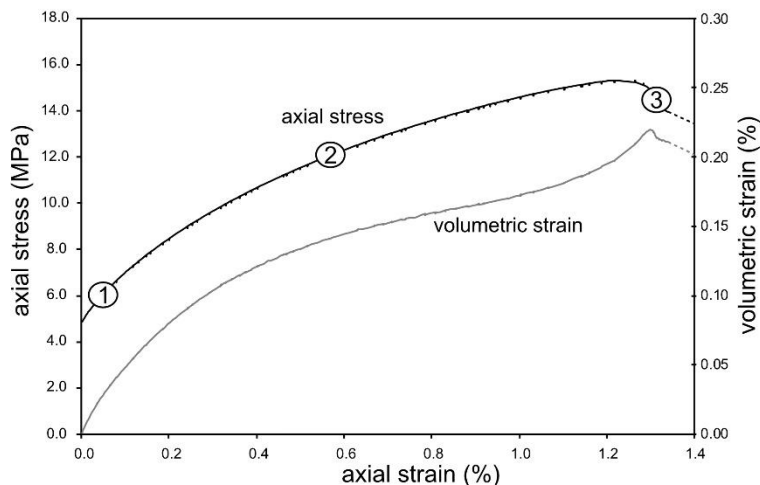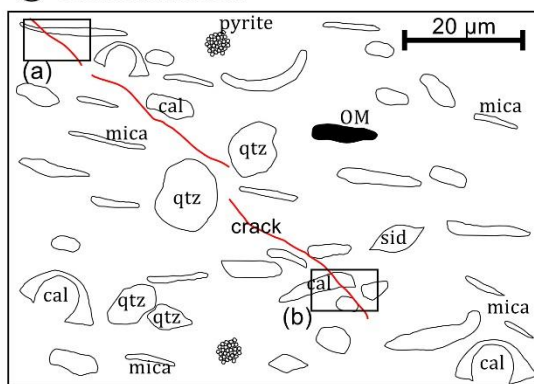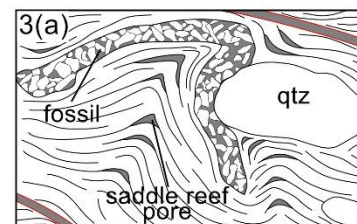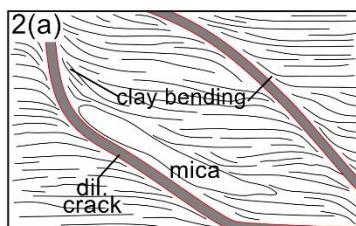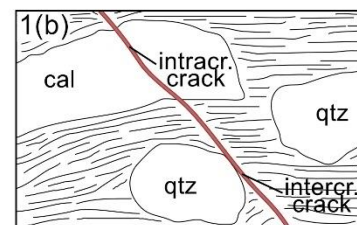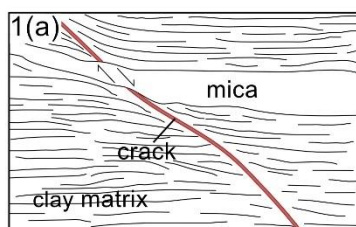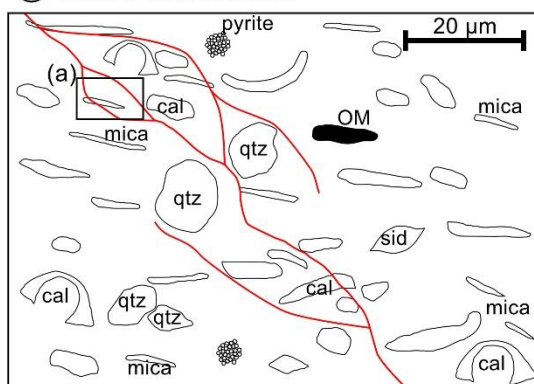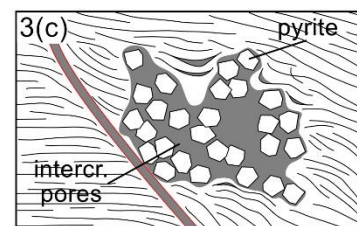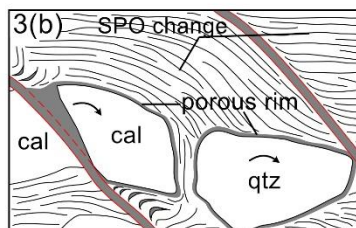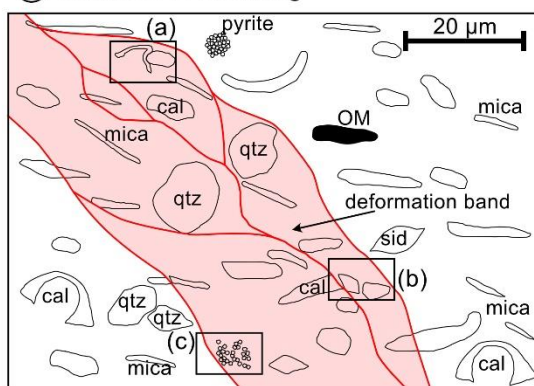
Figure 9: Deformation model for experimentally deformed OPA in a triaxial test consisting of different stages of damage accumulation: Stage 1 is associated to crack initiation where cracks form along a preferred oblique orientation. Stage 2 is characterised by micro-crack coalescence and the formation of anastomosing crack networks. Here, cracks dilate and clay particles bend towards the cracks. In stage 3, deformation bands show highly-deformed microstructures as strained fossils, delaminated clay aggregates, dilatant micro-cracks and a SPO change. Within these bands porosity is increased by saddle reed pores between clay layers, collapsed fossil shells, porous rims around larger grains and the formation of intracrystalline pores in pyrite aggregates.